Phase-Dependent MoS₂ Nanoflowers for Light-Driven Antibacterial Application

Chinmaya Mutalik, Dyah Ika Krisnawati, Shivaraj B. Patil, Muhamad Khafid, Didik Susetiyanto Atmojo, Puguh Santoso, Ssu-Chiao Lu, Di-Yan Wang,* and Tsung-Rong Kuo*

Cite This: *ACS Sustainable Chem. Eng.* 2021, 9, 7904–7912

Read Online

ACCESS | Metrics & More | Article Recommendations | Supporting Information

ABSTRACT: The metallic phase of 1T-MoS₂ nanoflowers (NFs) and the semiconducting phase of 2H-MoS₂ NFs were prepared by a facile solvothermal and combustion method. The antibacterial activities, reactive oxygen species (ROS) generation, and light-driven antibacterial mechanism of metallic 1T-MoS₂ NFs and semiconducting 2H-MoS₂ NFs were demonstrated with the bacterium *Escherichia coli* (*E. coli*) under light irradiation. Results of the bacterial growth curve and ROS generation analyses revealed higher light-driven antibacterial activity of metallic 1T-MoS₂ NFs compared to semiconducting 2H-MoS₂ NFs. Electron paramagnetic resonance (EPR) spectroscopy demonstrated that the ROS of the superoxide anion radical ·O₂⁻ was generated due to the incubation of 1T-MoS₂ NFs and *E. coli* with light irradiation. Furthermore, *E. coli* incubated with metallic 1T-MoS₂ NFs exhibited significant damage to the bacterial cell walls, complete bacterial destruction, and abnormal elongation after light irradiation. The light-driven antibacterial mechanism of metallic 1T-MoS₂ NFs was examined, and we found that, under light irradiation, photoinduced electrons were generated by metallic 1T-MoS₂ NFs, and then the photoinduced electrons reacted with oxygen to generate superoxide anion radical which induced bacterial death. For semiconducting 2H-MoS₂ NFs, photoinduced electrons and holes rapidly recombined resulting in a decrease in ROS generation which diminished the light-driven antibacterial activity.

KEYWORDS: *Metallic 1T-MoS₂, Semiconducting 2H-MoS₂, Photoactivity, Reactive oxygen species, Superoxide anion radical*
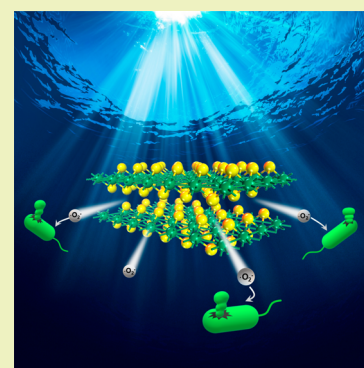
INTRODUCTION

Antibiotic-resistant bacteria are on the rise globally, causing extensive public health concerns.[1−3] Growing microbial defiance of antibiotics is one of the unanswered challenges of this era. The growth rate of microbial resistance to antibiotics is imprecise, but nearly 10 million deaths per annum are forecast to occur before 2050 worldwide.[4−6] To fight antimicrobial-resistant bacteria, alternative approaches derived from the use of photocatalysts such as carbon-based, metallic, or semiconducting nanomaterials are being explored.[7−14] Extensive work has been carried out in photocatalysts including titanium dioxide (TiO₂) based nanomaterials, graphene-based nanostructures, and plasmonic metal nanocrystals as light-activated antibacterial agents.[15−19] For example, light-activated TiO₂ nanomaterials were developed with dopants of nitrogen and bismuth, which kill the biofilms of *Streptococcus sanguinis* and *Actinomyces naeslundii* when irradiated with visible light.[20] Reduced graphene oxide (GO)−copper oxide nanostructures have been developed against *Escherichia coli* (*E. coli*) and *Staphylococcus aureus* (*S. aureus*) utilizing the synergetic effect of continuous efflux of copper ions and long-term reactive oxygen species (ROS) produced under light irradiation.[21] Plasmonic silica-coated Au−Ag nanocages were fabricated as wide-ranging antimicrobial media on *S. aureus* and *E. coli* via their photothermal properties

and steady and consistent efflux of Ag ions upon near-infrared irradiation.[22] Many previous reports proved that photocatalysts exhibit promising potential as antibacterial agents based on their photothermal effects and light-induced ROS production. However, the development of light-activated antibacterial nanomaterials with easy preparation, low cost, and high photoactivity is still an urgent task to combat bacterial infections.

Recently, multiphasic molybdenum disulfide (MoS₂) nanomaterials with photoactivities were fabricated for applications in energy production and storage.[23−28] Moreover, functionalized MoS₂ nanomaterials were also utilized as light-driven antibacterial materials. For example, exfoliated MoS₂ displayed a higher antimicrobial capacity compared to flamed exfoliated MoS₂ on planktonic cells, which was attributed to the higher electron conductivity of exfoliated MoS₂ leading to increased ROS generation.[29] Recently, pyramid-shaped MoS₂@Ag and MoS₂@copper films have shown that water disinfection under
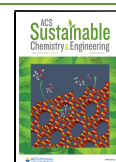
light irradiation against *E. coli* exhibited high antibacterial efficiency with concentration levels of 0.7 and 1.6 mg/L, respectively.[30,31] MoS_2–ZnO-reduced GO nanocomposites displayed high antibacterial activity under light irradiation against *S. aureus* and *E. coli* because photoexcited electrons from ZnO nanoparticles can be delivered to MoS_2 through the substrate of reduced GO to eliminate electron–hole pair combinations.[32] Bare Bi_2WO_6 and MoS_2 have lower separation efficiencies for photogeneration compared to MoS_2 quantum dot interspersed Bi_2WO_6 heterostructures and enhanced visible-light-driven photocatalytic detoxification and disinfection of wastewater.[33] Polyethylene glycol functionalized MoS_2 nanoflowers (NFs) were used for the quick and effective eradication of ampicillin-resistant *E. coli* and endospore-forming *Bacillus subtilis* by a photothermal effect and peroxidase catalytic activity.[34] Great efforts have been made to design and demonstrate outstanding light-induced antibacterial activities of MoS_2-related nanomaterials. However, there have been rare efforts to study and compare the potential antibacterial activities and mechanisms under light irradiation with two directly synthesized phases $1T$-MoS_2 NFs and $2H$-MoS_2 NFs.[35]

A simple solvothermal and combustion method was used to prepare $1T$ and $2H$ phases of MoS_2 NFs in this analysis. Powder X-ray diffraction (XRD), X-ray photoelectron spectroscopy (XPS), Raman spectroscopy, scanning electron microscopy (SEM), transmission electron microscopy (TEM), energy-dispersive X-ray (EDX) spectroscopy, and UV–visible spectroscopy were used to substantiate the skeletal properties of $1T$ and $2H$ phases of MoS_2 NFs. Furthermore, we investigated and compared the antibacterial activities and intercellular ROS generation of $1T$ and $2H$ phases of MoS_2 NFs against *E. coli* under light irradiation. Detailed mechanisms of the light-driven antibacterial effects by the two phases $1T$- and $2H$-MoS_2 NFs are also explored and demonstrated.

■ MATERIALS AND METHODS

Chemicals. Molybdic acid and thiourea were purchased from Acros Organics USA. Glycerol (Honeywell), Luria broth, ampicillin, LB agar Miller (Bioshop), agar-A (Biobasic), 2′,7′-dichlorofluorescein diacetate (DCFH-DA) (Sigma-Aldrich), and bisBenzimide H-33342 trihydrochloride trihydrate (Hoechst 33342) (Biotium) were purchased and used without further purification.

Syntheses of the Two Phases of $1T$-MoS_2 NFs and $2H$-MoS_2 NFs. $1T$-MoS_2 NFs were synthesized using a solvothermal process. Molybdic acid (0.005 M) and thiourea (0.0125 M) were used as precursors. In a nutshell, both precursors were dissolved in 40 mL of distilled water, stirred for 30 min to produce a homogeneous solution, and then moved to a 100 mL autoclave reactor. Carbon fiber paper (CeTech) with dimensions of 7 cm length and 2 cm width was introduced into the autoclave reactor. Further, the oven (JOV-40) was set to 180 °C, and the as-prepared autoclave reactor was put into the oven for 24 h. Furthermore, the autoclave reactor was taken out and left to cool until room temperature was attained. $1T$-MoS_2 NFs adhered to the carbon fiber paper were cleaned with deionized water and ethanol, left to dry overnight at 60 °C, and used for further applications. For the synthesis of $2H$-MoS_2 NF, $1T$-MoS_2 NFs were first prepared, and then $1T$-MoS_2 NFs were annealed in an incinerator (Thermofisher Lindberg Blue M) above 300 °C for 1 h to get $2H$-MoS_2 NFs. As-prepared $2H$-MoS_2 NFs were used for further experiments.

Material Characterization. SEM and TEM were performed with JEOL JSM-7800F and Hitachi HT-7700 instruments, respectively. For TEM samples of the two phases $1T$ and $2H$ of MoS_2 NFs were sonicated in deionized water and then dropped onto a copper mesh,

dried, and used for imaging. A JEOL 2100F was used for high-resolution transmission electron microscopic (HR-TEM) images. Also, a Rigaku Miniflex 600 with Cu Kα radiation was used to study structural details by X-ray diffraction. X-ray photoemission spectroscopic (XPS) analysis was performed at the National Synchrotron Radiation Research Center (NSRRC) SPEM terminal (BL09A).[36] The high-resolution XPS spectra were obtained at 320 eV photon energy for the $1T$ and $2H$ phases of MoS_2 NFs. An Olympus objective (16 mW) was used to record Raman measurements. Raman spectra were acquired by using Plan N and an Olympus objective at 16 mW. The skeletal features of the $1T$-MoS_2 NFs and $2H$-MoS_2 NFs were confirmed by SEM, TEM, XRD, and Raman spectroscopy. A JASCO-V770 spectrophotometer was used in this study to evaluate and validate the absorption properties of $1T$-MoS_2 NFs and $2H$-MoS_2 NFs.

Antibacterial Activity Assay. Bacterial solutions were prepared using 3 mL of LB broth medium, 300 μL of ampicillin, and 150 μL of an *E. coli* solution. The bacteria were cultured in LB broth medium in an incubator (YIHDER LM-80DR) with shaking at a speed of 160 rpm for 18 h at 37 °C. In addition, the bacterial solution was used to evaluate the antibacterial properties of $1T$-MoS_2 NFs and $2H$-MoS_2 NFs (both 0.4 mg/L). Simulated solar AM1.5 light (xenon lamp, Enlitech LH150) was applied as the light source. For the antibacterial test, the absorbance of the *E. coli* in LB medium was adjusted to 0.1 at 600 nm. $1T$-MoS_2 NFs and $2H$-MoS_2 NFs coated onto the carbon fiber paper were immersed in the LB medium containing *E. coli* and then exposed to simulated light for 4 min. Thereafter, the LB medium containing *E. coli* was cultured at 37 °C in a shaker at 160 rpm, and the absorbance of the LB medium containing *E. coli* was obtained every 30 min for 3 h.

ROS Generation Assay. ROS generation by $1T$-MoS_2 NFs and $2H$-MoS_2 NFs was obtained and confirmed using EPR spectroscopy and a 2′,7-dichlorodihydrofluorescein diacetate (H_2DCFDA) ROS test. To explain in brief, in a 96 well plate, 10 μM DCFH-DA and 1 μg/mL Hoechst 33342 underwent addition individually to the LB medium containing *E. coli*. Further, the medium was incubated and shaken at 200 rpm for 20–30 min at 37 °C. The medium underwent centrifugation at $10^4 g$ for 2 min (Thermo Scientific Heraeus Multifuge x1r), then cleaned once with double distilled water, and finally suspended in deionized water. The dichlorodihydrofluorescein was excited at a wavelength of 488 nm, and the fluorescence intensity was measured at a wavelength of 525 nm. For Hoechst 33342, the wavelengths of excitation and emission were respectively set at 350 and 461 nm. The fluorescence intensities were measured with a microplate reader (Thermo Varioskan Flash). All statistical data were managed and plotted by using Origin 8.5pro software.

■ RESULTS AND DISCUSSION

Characterization of $1T$-MoS_2 NFs and $2H$-MoS_2 NFs. $1T$-MoS_2 NFs and $2H$-MoS_2 NFs were obtained by a solvothermal method and combustion process. The morphologies and compositions of $1T$-MoS_2 NFs and $2H$-MoS_2 NFs were validated by SEM, TEM, HR-TEM, EDX analysis, and EDX mapping. As displayed in SEM images of Figure 1a,d, the morphologies of both $1T$-MoS_2 NFs and $2H$-MoS_2 NFs were recognized as woven flowerlike structures composed by multilayered MoS_2 nanosheets. On the basis of SEM images, the average sizes of the multilayered $1T$-MoS_2 NFs and $2H$-MoS_2 NFs were calculated to be ca. 400–800 nm. Furthermore, EDX spectra of $1T$-MoS_2 NFs and $2H$-MoS_2 NFs were measured as shown in Figures S1 and S2, respectively. The weights and atom percentages of $1T$-MoS_2 NFs and $2H$-MoS_2 NFs were also calculated by EDX spectra as demonstrated in Tables S1 and S2. EDX analysis showed that $1T$-MoS_2 NFs consisted of molybdenum (Mo, 64.26 wt %) and sulfur (S, 35.74 wt %). In addition, $2H$-MoS_2 NFs consisted of Mo (63.35 wt %) and S (36.65 wt %). EDX
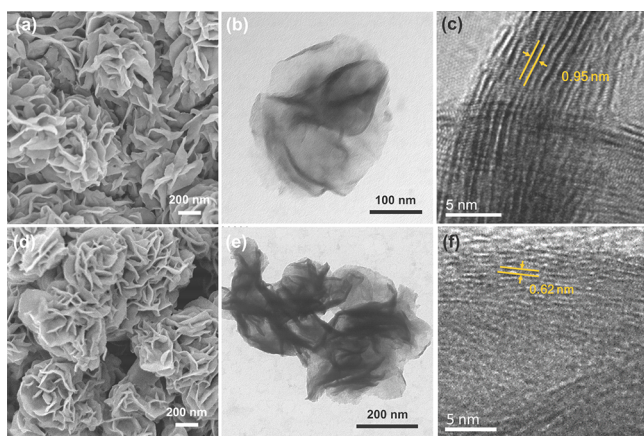
Figure 1. (a) SEM, (b) TEM, and (c) HR-TEM images of 1T-MoS$_2$-NFs. (d) SEM, (e) TEM, and (f) HR-TEM images of 2H-MoS$_2$-NFs.

analyses showed that the compositions were not significantly different between 1T-MoS$_2$ NFs and 2H-MoS$_2$ NFs. To further investigate the elemental distributions, EDX mapping was performed to characterize 1T-MoS$_2$ NFs and 2H-MoS$_2$ NFs. As shown in Figure S3a−c, the SEM images of 1T-MoS$_2$ NFs and the corresponding EDX elemental distribution images showed that the elements Mo and S were homogeneously distributed in 1T-MoS$_2$ NFs. In Figure S3d−f, the SEM images and the EDX element distribution images also show the homogeneous distribution of the elements of Mo and S in 2H-MoS$_2$ NFs. Moreover, in TEM images of Figure 1b,e, the nanosheet structures of multilayered 1T-MoS$_2$ NFs and 2H-MoS$_2$ NFs can be clearly seen.[37−39] Furthermore, HR-TEM images of 1T-MoS$_2$ NFs and 2H-MoS$_2$ NFs were also analyzed to confirm the structural information. Figure 1c shows fringe

patterns with 1T-MoS$_2$ NFs with a *d*-spacing of 0.95 nm corresponding to the (002) plane of the 1T-phase of MoS$_2$. In Figure 1f, the *d*-spacing of 2H-MoS$_2$ NFs was 0.62 nm corresponding to the distance between the layers of the (002) plane for the 2H phasing.[35,40] Figure S4a,b shows the electron diffraction (ED) patterns of 1T-MoS$_2$ NFs and 2H-MoS$_2$. Furthermore, structural characterizations such as SEM, EDX, TEM, HR-TEM, and EDX mapping verified the efficient hydrothermal and annealing process syntheses of 1T-MoS$_2$ NFs and 2H-MoS$_2$ NFs with homogeneous Mo and S element distributions.

XRD and XPS Studies of 1T-MoS$_2$ NFs and 2H-MoS$_2$ NFs. To characterize the gem structure, XRD was utilized to look at 1T-MoS$_2$ NFs and 2H-MoS$_2$ NFs. As shown in Figure 2a, for 1T-MoS$_2$ NFs noteworthy peaks appear at 9.20 and 18.00° separately compared to the (002) and (004) planes of 1T-MoS$_2$. As shown in Figure 2b, 2H-MoS$_2$ NFs were proven by the arrangement of a peak at 14.40° ordered to the (002) plane. XRD peaks of 1T-MoS$_2$ NFs and 2H-MoS$_2$ NFs were insinuated by JCPDF No. 37-1492. XRD illustrated that 1T-MoS$_2$ NFs were effectively synthesized by means of the aqueous strategy, and after that the as-synthesized 1T-MoS$_2$ NFs were advance strengthened to get 2H-MoS$_2$ NFs. Past reports demonstrated that 1T-MoS$_2$ NFs showed metastability, an octahedral frame, and metallic properties. On the other hand, 2H-MoS$_2$ NFs appeared to show improved thermody-namic steadiness, a hexagonal frame, and semiconductor properties.[41−43]

Parts c and d of Figure 2 show X-ray photoelectron spectrocopic studies of 1T-MoS$_2$ NFs and 2H-MoS$_2$ NFs with respect to Mo 3d and S 2p spectra, respectively. In Figure 2c, 1T-MoS$_2$ NFs and 2H-MoS$_2$ NFs were validated by two distinct peaks of Mo 3d$_{5/2}$ and Mo 3d$_{3/2}$, respectively. The
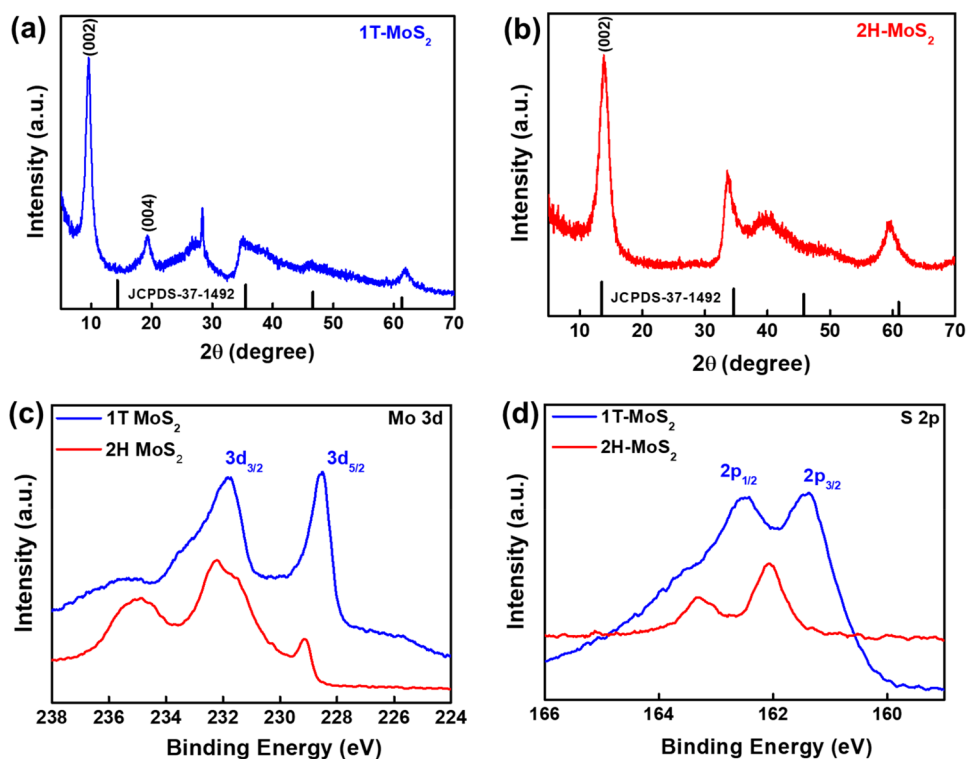
Figure 2. XRD patterns of (a) 1T-MoS$_2$ NFs and (b) 2H-MoS$_2$ NFs. XPS spectra of 1T-MoS$_2$ NFs and 2H-MoS$_2$ NFs with respect to (c) Mo 3d and (d) S 2p.
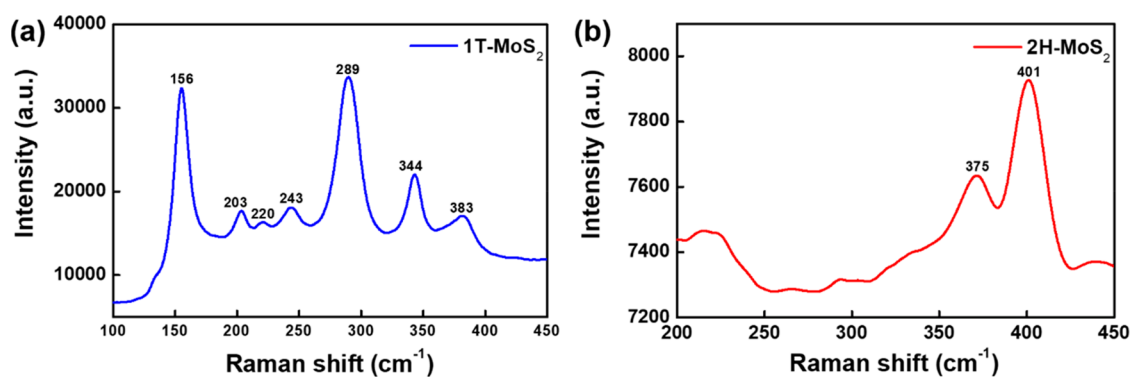
Figure 3. Raman spectra of (a) 1T-MoS$_2$ NFs and (b) 2H-MoS$_2$ NFs.
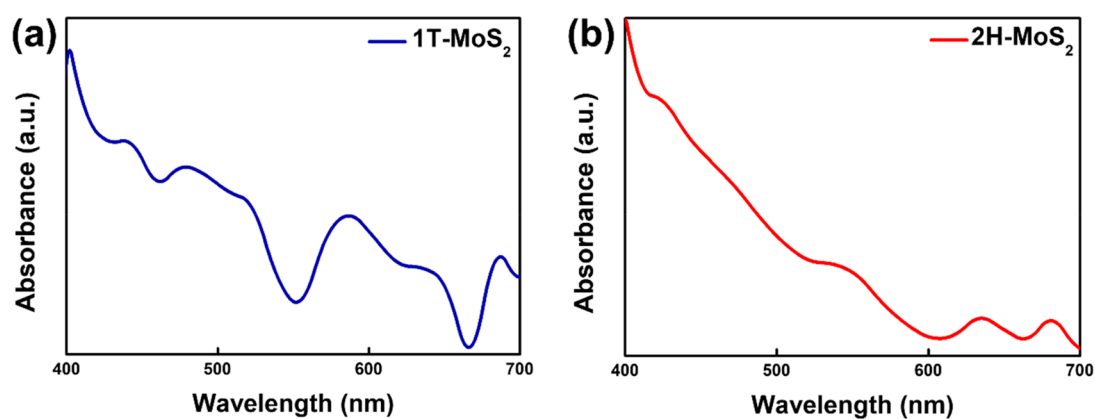
Figure 4. Absorption spectra of (a) 1T-MoS$_2$ NFs and (b) 2H-MoS$_2$ NFs.

peaks of Mo 3d$_{5/2}$ and Mo 3d$_{3/2}$ for 1T-MoS$_2$ NFs showed lower binding energies than those of 2H-MoS$_2$ NFs. As shown in Figure 2d, the XPS spectra showed two characteristic peaks of S 2p$_{1/2}$ and S 2p$_{3/2}$ for 1T-MoS$_2$ NFs and 2H-MoS$_2$ NFs, respectively. S 2p$_{1/2}$ and S 2p$_{3/2}$ of 1T-MoS$_2$ NFs also showed the decrease of binding energies compared to those of 2H-MoS$_2$ NFs. The decrease in the binding energies of Mo and S in 1T-MoS$_2$ NFs compared to those of 2H-MoS$_2$ NFs could be due to an increase in the electron densities of Mo and S atoms, respectively. Figure S5a−d shows deconvoluted and fitted spectra for Mo and S atoms in 1T-MoS$_2$ NFs and 2H-MoS$_2$ NFs individually and supported by reported literature.[44−48] These important properties of 1T-MoS$_2$ NFs and 2H-MoS$_2$ NFs were utilized for light-driven antibacterial applications.

Raman Spectroscopy of 1T-MoS$_2$ NFs and 2H-MoS$_2$ NFs. Raman spectroscopy was used to validate and verify the structural properties of 1T-MoS$_2$ NFs and 2H-MoS$_2$ NFs. In Figure 3a, a low-energy Raman peak of 1T-MoS$_2$ NFs located at 156 cm^{-1} was identified as a J$_1$ phonon mode, indicating Mo−Mo atoms arranging in and extending out of a lattice site. The peaks of 1T-MoS$_2$ NFs at 203, 220, and 243 cm^{-1} were attributed to a J$_2$ phonon mode, which indicates Mo−S atoms stretching in and out of the layers. The peak of the E$_g$ mode at 289 cm^{-1} also corresponded to the stretching of Mo−S atoms and their arrangement in the lattice. The peak of the J$_3$ mode at 344 cm^{-1} was attributed to the perpendicular motion of Mo−Mo atoms in the lattice site. The two phonon modes of E$_{2g}$ and A$_{1g}$ (383 cm^{-1}) corresponded to vibrations of Mo−Mo atoms, S−Mo−S atoms, and Mo−S atoms at comparatively higher energies in the lattice sites of 1T-MoS$_2$ NFs. The two modes of E$_{2g}$ and A$_{1g}$ peaks coincided with each other, which can be

attributed to manipulations of the layers in 1T-MoS$_2$ NFs by weak physical forces. In the Raman spectrum of 2H-MoS$_2$ NFs (Figure 3b), the two phonon modes of E$_{2g}$ (375 cm^{-1}) and A$_{1g}$ (401 cm^{-1}) corresponded to the vibrations of Mo−Mo atoms, S−Mo−S atoms, and Mo−S atoms at analogously larger energies in the lattice sites. Compared to 1T-MoS$_2$ NFs, the disappearance of lower energy Raman peaks in 2H-MoS$_2$ NFs was attributed to the superior structural symmetry of 2H-MoS$_2$ NFs.[49−57] To sum up, the results of Raman spectra confirmed the successful preparation of 1T-MoS$_2$ NFs and 2H-MoS$_2$ NFs.

UV−Vis Spectra of 1T-MoS$_2$ NFs and 2H-MoS$_2$ NFs. To investigate the optical properties, the absorption spectra of 1T-MoS$_2$ NFs and 2H-MoS$_2$ NFs were examined by UV−vis spectroscopy. As shown in Figure 4a, the UV−vis spectrum of 1T-MoS$_2$ NFs showed two prominent narrow peaks at wavelengths of 588 and 438 nm corresponding to the excitonic absorption.[58] As shown in Figure 4b, the UV−vis spectrum of 2H-MoS$_2$ NFs displayed four characteristic absorption bands including excitons (680 and 635 nm) and direct transitions from the valence band to the conduction band (540 and 423 nm) due to the semiconducting 2H-phase of 2H-MoS$_2$ NFs.[59] Compared with 2H-MoS$_2$ NFs, the absorption peaks at 680 and 635 nm of 1T-MoS$_2$ NFs can be attributed to the excitonic absorptions of 2H-MoS$_2$ NFs. Thus, 1T-MoS$_2$ NFs were assumed to mix with some 2H-MoS$_2$ NFs. Moreover, the metastable 1T-MoS$_2$ NFs were reported to be metallic and to have high conductive and photocatalytic properties.[60−62] Therefore, metallic 1T-MoS$_2$ NFs and semiconducting 2H-MoS$_2$ NFs were further used as light-activated antibacterial agents in this work. Overall, based on the results of UV−vis spectra, metallic 1T-MoS$_2$ NFs and semiconducting 2H-MoS$_2$

NFs each with broad absorption in the visible region were synthesized for the following antibacterial assay.

Light-Driven Antibacterial Activity of 1T-MoS$_2$ NFs and 2H-MoS$_2$ NFs. To evaluate their light-driven antibacterial activities, 1T-MoS$_2$ NFs and 2H-MoS$_2$ NFs were incubated individually with *E. coli* under solar light irradiation. As shown in Figure 5, an *E. coli* solution, 1T-MoS$_2$ NFs incubated with *E.*
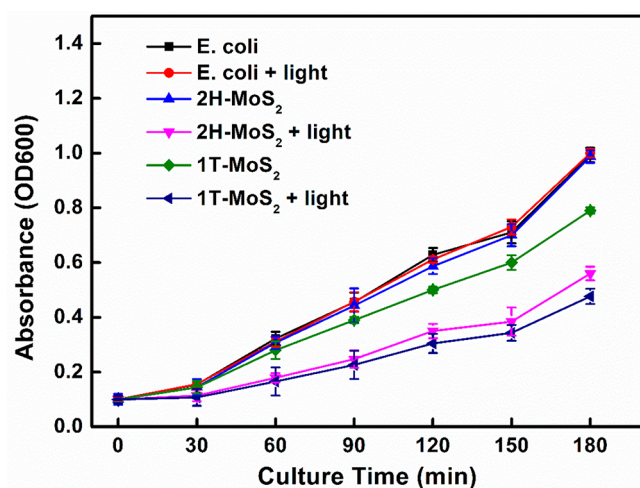
Figure 5. Growth curves of *E. coli*, 1T-MoS$_2$ nanoflowers (NFs), and 2H-MoS$_2$ NFs (both 0.4 mg/L) with and without light irradiation for 4 min. All data is provided as mean standard deviations, with $n = 3$ per category.

coli, and 2H-MoS$_2$ NFs incubated with *E. coli* were examined with and without light illumination. The growth curves of *E. coli* indicated no significant difference between the light-irradiated and nonirradiated conditions. However, without light irradiation, 2H-MoS$_2$ NFs exhibited minor antibacterial effect against *E. coli*. Most importantly, increased antibacterial efficiencies of 1T-MoS$_2$ NFs and 2H-MoS$_2$ NFs were obtained with light irradiation. Therefore, 1T-MoS$_2$ NFs were able to inhibit bacterial growth better than 2H-MoS$_2$ NFs under light irradiation. To further investigate the light-driven antibacterial efficiencies, ROS generated by 1T-MoS$_2$ NFs and 2H-MoS$_2$

NFs were separately measured with and without visible light irradiation.

Light-Driven ROS Production by 1T-MoS$_2$ NFs and 2H-MoS$_2$ NFs. ROS measurements were carried out with an H$_2$DCFDA assay. ROS measurements of the blank (*E. coli*), 1T-MoS$_2$ NFs incubated with *E. coli*, and 2H-MoS$_2$ NFs incubated with *E. coli* were evaluated under light irradiation and no-light conditions. Figure 6a shows that there were no substantial changes in ROS output for *E. coli* with and without light irradiation, corresponding to *E. coli* bacterial growth curves. In comparison to the control, the relative ROS levels of 1T-MoS$_2$ NFs and 2H-MoS$_2$ NFs were 3.34-fold and 1.68-fold, respectively, without light irradiation (*E. coli* without light irradiation). In comparison to 2H-MoS$_2$ NFs, 1T-MoS$_2$ NFs have more active sites, according to a previous report.[63] Therefore, with more active sites, 1T-MoS$_2$ NFs produced higher ROS than 2H-MoS$_2$ NFs without light irradiation. With light irradiation, 1T-MoS$_2$ NFs and 2H-MoS$_2$ NFs showed respective 5.89-fold and 3.85-fold increases in ROS production. Results of ROS measurements indicated that 1T-MoS$_2$ NFs generated higher ROS compared to 2H-MoS$_2$ NFs under light irradiation. According to the results of their bacterial growth curves, 1T-MoS$_2$ NFs had better light-induced antibacterial activity than 2H-MoS$_2$ NFs with higher ROS output. Previous studies demonstrated that the production of ROS, such as $^\bullet$O$_2^{2-}$, $^\bullet$OH, and $^\bullet$O$_2^-$, causes consequent deterioration of microbial cell walls.[64−66] Electron paramagnetic resonance (EPR) spectroscopy was used to detect and identify free radicals and other species with unpaired electrons generated by 1T-MoS$_2$ NFs incubated with *E. coli* after light irradiation to further investigate ROS development. The EPR spectrum of 1T-MoS$_2$ NFs incubated with *E. coli* after light illumination revealed the formation of the superoxide anion radical $^\bullet$O$_2^-$, as shown in Figure 6b.[67] The EPR spectrum of 2H-MoS$_2$ NFs incubated with *E. coli* after light irradiation revealed no significant production of the superoxide anion radical $^\bullet$O$_2^-$ (Figure S6). Overall, results of ROS measurements indicated that 1T-MoS$_2$ NFs showed advanced ROS generation and bacteriostasis under light irradiation compared to 1T-MoS$_2$ NFs without light irradiation and 2H-MoS$_2$ NFs under light and no-light irradiation.
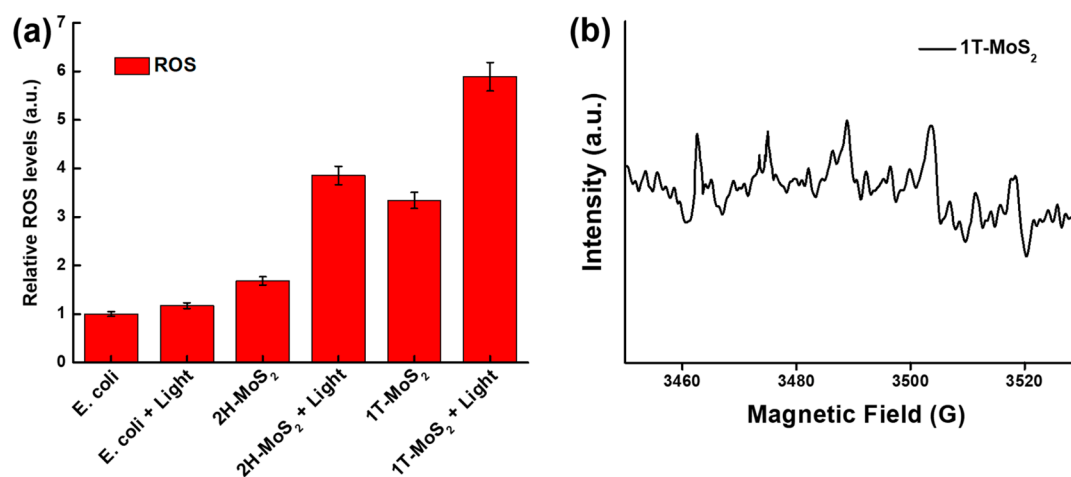
Figure 6. (a) Without light irradiation, the amount of reactive oxygen species in *E. coli* was set to the normal value (1.0). *E. coli* relative ROS levels were determined under light irradiation and no-light irradiation after incubation with 1T-MoS$_2$ NFs and 2H-MoS$_2$ NFs. (b) After light irradiation, EPR range of the superoxide radical adduct of 5,5-dimethyl-1-pyrroline *N*-oxide (DMPO) and 1T-MoS$_2$ NFs incubated with *E. coli*.

Furthermore, SEM images of *E. coli* incubated with 1T-MoS$_2$ NFs were examined with and without light irradiation to help ROS generation by 1T-MoS$_2$ NFs. The SEM picture of *E. coli* incubated with 1T-MoS$_2$ NFs without light irradiation in Figure 7a shows no significant harm. Figure 7b shows
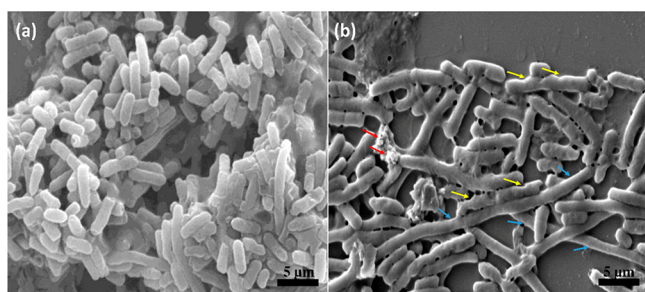
Figure 7. (a) *E. coli* incubated with 1T-MoS$_2$ NFs (no light irradiation) and (b) *E. coli* incubated with 1T-MoS$_2$ NFs with light irradiation (SEM images). Yellow arrows indicate bacterial cell membrane rupture, red arrows indicate destruction of bacteria, and blue arrows indicate abnormal elongation of bacteria without division.

substantial bacterial cell wall damage (yellow arrows), complete bacterial destruction (red arrows), and irregular *E. coli* elongation (blue arrows). The HR-SEM image of *E. coli* incubated with 1T-MoS$_2$ NFs with light irradiation was provided as Figure S7. Apparently, under light irradiation, the increased ROS production by 1T-MoS$_2$ NFs caused inactivation of cell division Z-ring and penicillin-binding proteins, indicating short-term survival of *E. coli*.[68] The results indicated that, under light irradiation, 1T-MoS$_2$ NFs enhanced ROS production and revealed efficient antibacterial activity.

Light-Driven Antibacterial Activities of 1T-MoS$_2$ NFs and 2H-MoS$_2$ NFs Mechanisms. Under visible light (ca. 400−700 nm) irradiation, 1T-MoS$_2$ NFs and 2H-MoS$_2$ NFs were found to be photoactive.[69] Under light irradiation, metallic 1T-MoS$_2$ NFs were shown to produce more ROS than semiconducting 2H-MoS$_2$ NFs in this study. The superior light-driven antibacterial activity of 1T-MoS$_2$ NFs compared to 2H-MoS$_2$ NFs may be due to phase differences between the metallic and semiconducting phases. Previous reports demonstrated that metallic 1T-MoS$_2$ NFs produce photoelectrons under light irradiation by a photoelectronic effect.[70−72] The mechanism of the light-driven antibacterial activity of 1T-MoS$_2$ NFs appears to be that, with light irradiation, photoelectrons generated by metallic 1T-MoS$_2$ NFs further reacted with oxygen to generate superoxide ($^\bullet$O$_2^-$), as shown in Figure 8. Under light irradiation, the semiconducting 2H-MoS$_2$ NFs formed photoinduced electron−hole pairs. Recombination of photoinduced electron−hole pairs decreased the efficiency of the formation of ROS in semiconducting 2H-MoS$_2$ NFs, resulting in a decrease in light-driven antibacterial operation. As a result, metallic 1T-MoS$_2$ NFs have been shown to have higher light-driven antibacterial activity than semiconducting 2H-2 NFs. With superior photoactivity and ease of preparation, metallic 1T-MoS$_2$ NFs could be a promising light-driven antibacterial for applications in food security, water sanitation, and medical sterilization.

■ CONCLUSIONS

A solvothermal process and annealing system were used to successfully synthesize metallic 1T-MoS$_2$ NFs and semi-
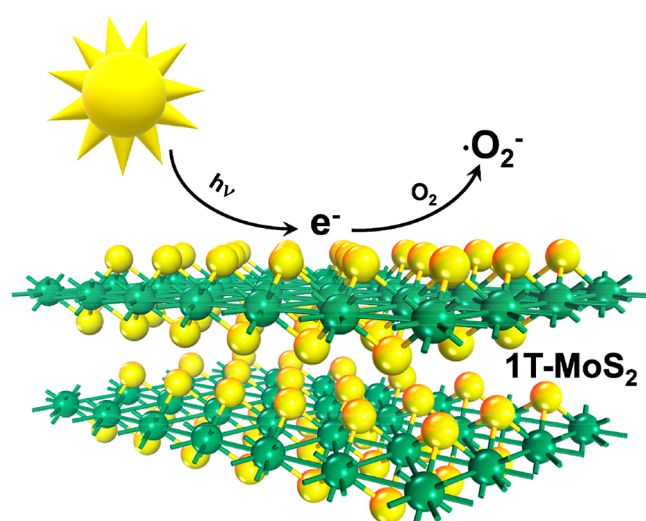
Figure 8. Schematic illustration of superoxide ($^\bullet$O$_2^-$) generation from 1T-MoS$_2$ NFs under light irradiation.

conducting 2H-MoS$_2$ NFs. SEM, TEM, HR-TEM, EDX, EDX mapping, XRD, XPS, Raman, and UV−vis spectroscopy were used to demonstrate the structural and optical properties of metallic 1T-MoS$_2$ NFs and semiconducting 2H-MoS$_2$ NFs. Furthermore, the antibacterial activities and ROS generation of metallic 1T-MoS$_2$ NFs and semiconducting 2H-MoS$_2$ NFs were evaluated and validated under no-light and light irradiation. Under light irradiation, metallic 1T-MoS$_2$ NFs were found to have higher antibacterial activity than semiconducting 2H-MoS$_2$ NFs based on the results of the bacterial growth curve and ROS generation. For ROS generation, metallic 1T-MoS$_2$ NFs activated by light irradiation were measured to have enhanced ROS production by a 5.89-fold increase compared to that of semiconducting 2H-MoS$_2$ NFs (3.85-fold increase) under light irradiation. With incubation of metallic 1T-MoS$_2$ NFs, *E. coli* exhibited significant damage to the cell walls, complete bacterial destruction, and abnormal elongation after light irradiation. The mechanism of the highly light-driven antibacterial activity of metallic 1T-MoS$_2$ NFs is that, under light irradiation, metallic 1T-MoS$_2$ NFs generate photoelectrons and then the photoelectrons further react with oxygen to generate superoxide to induce bacterial death. The semiconducting 2H-MoS$_2$ NFs formed photoinduced electron−hole pairs when exposed to light, and the recombination of the photoinduced electrons and holes decreased the output of ROS, reducing light-driven antibacterial activity. Our findings show that metallic 1T-MoS$_2$ NFs with excellent light-driven antibacterial activity could be a useful antibacterial agent in the near future.

■ ASSOCIATED CONTENT

ⓈI Supporting Information

The Supporting Information is available free of charge at https://pubs.acs.org/doi/10.1021/acssuschemeng.1c01868.

> EDX spectra of 1T-MoS$_2$ and 2H-MoS$_2$ NFs; SEM images of 1T-MoS$_2$ and 2H-MoS$_2$ NFs and EDX mapping of Mo and S; ED patterns of 1T-MoS$_2$ and 2H-MoS$_2$ NFs; deconvoluted and fitted XPS spectra of 1T-MoS$_2$ and 2H-MoS$_2$ NFs with respect to Mo 3d and S 2p; EPR spectrum of DMPO during 2H-MoS$_2$ NFs incubated with *E. coli* after light irradiation; *E. coli*

incubated with 1T-MoS$_2$ NFs with light irradiation; presence and composition of elements in 1T-MoS$_2$ and 2H-MoS$_2$ NFs (PDF)

■ **AUTHOR INFORMATION**

Corresponding Authors

Di-Yan Wang − *Department of Chemistry, Tunghai University, Taichung City 40704, Taiwan; Life Science Research Center, Tunghai University, Taichung City 40704, Taiwan;* orcid.org/0000-0003-3084-6050; Email: diyanwang@thu.edu.tw

Tsung-Rong Kuo − *International PhD Program in Biomedical Engineering, College of Biomedical Engineering and Graduate Institute of Nanomedicine and Medical Engineering, College of Biomedical Engineering, Taipei Medical University, Taipei 11031, Taiwan;* orcid.org/0000-0003-4937-951X; Email: trkuo@tmu.edu.tw

Authors

Chinmaya Mutalik − *International PhD Program in Biomedical Engineering, College of Biomedical Engineering, Taipei Medical University, Taipei 11031, Taiwan*

Dyah Ika Krisnawati − *Dharma Husada Nursing Academy, Kediri, East Java 64114, Indonesia*

Shivaraj B. Patil − *Department of Chemistry, Tunghai University, Taichung City 40704, Taiwan*

Muhamad Khafid − *Faculty of Nursing and Midwivery, Nahdlatul Ulama University of Surabaya, Surabaya 60243, Indonesia*

Didik Susetiyanto Atmojo − *Dharma Husada Nursing Academy, Kediri, East Java 64114, Indonesia*

Puguh Santoso − *Dharma Husada Nursing Academy, Kediri, East Java 64114, Indonesia*

Ssu-Chiao Lu − *Graduate Institute of Nanomedicine and Medical Engineering, College of Biomedical Engineering, Taipei Medical University, Taipei 11031, Taiwan; Taoyuan Municipal Nankan Senior High School, Taoyuan City 33850, Taiwan*

Complete contact information is available at:
https://pubs.acs.org/10.1021/acssuschemeng.1c01868

Notes

The authors declare no competing financial interest.

■ **REFERENCES**

(1) Cosgrove, S. E.; Sakoulas, G.; Perencevich, E. N.; et al. Comparison of mortality associated with methicillin-resistant and methicillin-susceptible staphylococcus aureus bacteremia: A meta-analysis. *Clin. Infect. Dis.* **2003**, *36*, 53−59.

(2) Schwaber, M. J.; Carmeli, Y. Mortality and delay in effective therapy associated with extended-spectrum β-lactamase production in enterobacteriaceae bacteraemia: A systematic review and meta-analysis. *J. Antimicrob. Chemother.* **2007**, *60*, 913−920.

(3) Arias, C. A.; Murray, B. E. Antibiotic-resistant bugs in the 21st century-a clinical super-challenge. *N. Engl. J. Med.* **2009**, *360*, 439−443.

(4) De Kraker, M. E.; Davey, P. G.; Grundmann, H.; et al. Mortality and hospital stay associated with resistant staphylococcus aureus and Escherichia coli bacteremia: Estimating the burden of antibiotic resistance in europe. *PLoS Med.* **2011**, *8*, e1001104.

(5) de Kraker, M. E.; Stewardson, A. J.; Harbarth, S. Will 10 million people die a year due to antimicrobial resistance by 2050? *PLoS Med.* **2016**, *13*, e1002184.

(6) Stewardson, A. J.; Allignol, A.; Beyersmann, J.; et al. The health and economic burden of bloodstream infections caused by antimicrobial-susceptible and non-susceptible enterobacteriaceae and staphylococcus aureus in european hospitals, 2010 and 2011: A multicentre retrospective cohort study. *Eurosurveillance* **2016**, *21*, 30319.

(7) Chang, K.; Hai, X.; Pang, H.; et al. Targeted synthesis of 2H- and 1T-phase MoS$_2$ monolayers for catalytic hydrogen evolution. *Adv. Mater.* **2016**, *28*, 10033−10041.

(8) Yougbaré, S.; Chou, H.-L.; Yang, C.-H.; et al. Facet-dependent gold nanocrystals for effective photothermal killing of bacteria. *J. Hazard. Mater.* **2021**, *407*, 124617.

(9) Hsiao, Y.-C.; Jheng, P.-R.; Nguyen, H. T.; et al. Photothermal-irradiated polyethyleneimine-polypyrrole nanopigment film-coated polyethylene fabrics for infrared-inspired with pathogenic evaluation. *ACS Appl. Mater. Interfaces* **2021**, *13*, 2483−2495.

(10) Lu, K.-Y.; Jheng, P.-R.; Lu, L.-S.; et al. Enhanced anticancer effect of ROS-boosted photothermal therapy by using fucoidan-coated polypyrrole nanoparticles. *Int. J. Biol. Macromol.* **2021**, *166*, 98−107.

(11) Yougbaré, S.; Mutalik, C.; Krisnawati, D. I.; et al. Nanomaterials for the photothermal killing of bacteria. *Nanomaterials* **2020**, *10*, 1123.

(12) Chang, T.-K.; Cheng, T.-M.; Chu, H.-L.; et al. Metabolic mechanism investigation of antibacterial active cysteine-conjugated gold nanoclusters in escherichia coli. *ACS Sustainable Chem. Eng.* **2019**, *7*, 15479−15486.

(13) Yougbare, S.; Chang, T.-K.; Tan, S.-H.; et al. Antimicrobial gold nanoclusters: Recent developments and future perspectives. *Int. J. Mol. Sci.* **2019**, *20*, 2924.

(14) Chen, H.; Wang, B.; Gao, D.; et al. Broad-spectrum antibacterial activity of carbon nanotubes to human gut bacteria. *Small* **2013**, *9*, 2735−2746.

(15) Mutalik, C.; Wang, D.-Y.; Krisnawati, D. I.; et al. Light-activated heterostructured nanomaterials for antibacterial applications. *Nanomaterials* **2020**, *10*, 643.

(16) Cho, E. C.; Ciou, J. H.; Zheng, J. H.; et al. Fullerene c-70 decorated TiO$_2$ nanowires for visible-light-responsive photocatalyst. *Appl. Surf. Sci.* **2015**, *355*, 536−546.

(17) Gao, Y.; Wang, X.; Li, X.; et al. An antibacterial composite film based on cellulose acetate/TiO$_2$ nanoparticles. *New J. Chem.* **2020**, *44*, 20751−20758.

(18) Zhang, X. Y.; Zhang, G. N.; Chai, M. Z.; et al. Synergistic antibacterial activity of physical-chemical multi-mechanism by TiO$_2$ nanorod arrays for safe biofilm eradication on implant. *Bioact. Mater.* **2021**, *6*, 12−25.

(19) Mutalik, C.; Hsiao, Y.-C.; Chang, Y.-H.; et al. High uv-vis-nir light-induced antibacterial activity by heterostructured TiO$_2$-FeS$_2$ nanocomposites. *Int. J. Nanomed.* **2020**, *15*, 8911−8920.

(20) Nagay, B. E.; Dini, C.; Cordeiro, J. M.; et al. Visible-light-induced photocatalytic and antibacterial activity of TiO$_2$ codoped with nitrogen and bismuth: New perspectives to control implant-biofilm-related diseases. *ACS Appl. Mater. Interfaces* **2019**, *11*, 18186−18202.

(21) Yang, Z.; Hao, X.; Chen, S.; et al. Long-term antibacterial stable reduced graphene oxide nanocomposites loaded with cuprous oxide nanoparticles. *J. Colloid Interface Sci.* **2019**, *533*, 13−23.

(22) Wu, S.; Li, A.; Zhao, X.; et al. Silica-coated gold−silver nanocages as photothermal antibacterial agents for combined anti-infective therapy. *ACS Appl. Mater. Interfaces* **2019**, *11*, 17177−17183.

(23) Acerce, M.; Voiry, D.; Chhowalla, M. Metallic 1T phase MoS_2 nanosheets as supercapacitor electrode materials. *Nat. Nanotechnol.* **2015**, *10*, 313−318.

(24) Tu, C. C.; Peng, P. W.; Lin, L. Y. Weight ratio effects on morphology and electrocapacitive performance for the MoS_2/polypyrrole electrodes. *Appl. Surf. Sci.* **2018**, *444*, 789−799.

(25) Karunakaran, S.; Pandit, S.; Basu, B.; et al. Simultaneous exfoliation and functionalization of 2H-MoS_2 by thiolated surfactants: Applications in enhanced antibacterial activity. *J. Am. Chem. Soc.* **2018**, *140*, 12634−12644.

(26) Zhang, Y.; Mu, Z.; Yang, C.; et al. Rational design of mxene/1T-2H MoS_2-c nanohybrids for high-performance lithium−sulfur batteries. *Adv. Funct. Mater.* **2018**, *28*, 1707578.

(27) Fan, X.; Xu, P.; Zhou, D.; et al. Fast and efficient preparation of exfoliated 2H MoS_2 nanosheets by sonication-assisted lithium intercalation and infrared laser-induced 1T to 2H phase reversion. *Nano Lett.* **2015**, *15*, 5956−5960.

(28) Ramakrishna Matte, H. S. S.; Gomathi, A.; Manna, A. K.; Late, D. J.; Datta, R.; Pati, S. K.; Rao, C. N. R. MoS_2 and WS_2 analogues of graphene. *Angew. Chem., Int. Ed.* **2010**, *49*, 4059−4062.

(29) Fan, J.; Li, Y.; Nguyen, H. N.; et al. Toxicity of exfoliated-MoS_2 and annealed exfoliated-MoS_2 towards planktonic cells, biofilms, and mammalian cells in the presence of electron donor. *Environ. Sci.: Nano* **2015**, *2*, 370−379.

(30) Liu, C.; Kong, D.; Hsu, P.-C.; et al. Rapid water disinfection using vertically aligned MoS_2 nanofilms and visible light. *Nat. Nanotechnol.* **2016**, *11*, 1098−1104.

(31) Cheng, P.; Zhou, Q.; Hu, X.; et al. Transparent glass with the growth of pyramid-type MoS_2 for highly efficient water disinfection under visible-light irradiation. *ACS Appl. Mater. Interfaces* **2018**, *10*, 23444−23450.

(32) Priyadharsan, A.; Shanavas, S.; Vasanthakumar, V.; Balamuralikrishnan, B.; Anbarasan, P. M. Synthesis and investigation on synergetic effect of rGO-ZnO decorated MoS2 microflowers with enhanced photocatalytic and antibacterial activity. *Colloids Surf., A* **2018**, *559*, 43−53.

(33) Meng, X.; Li, Z.; Zeng, H.; et al. MoS_2 quantum dots-interspersed Bi_2WO_6 heterostructures for visible light-induced detoxification and disinfection. *Appl. Catal., B* **2017**, *210*, 160−172.

(34) Yin, W.; Yu, J.; Lv, F.; et al. Functionalized nano-MoS2 with peroxidase catalytic and near-infrared photothermal activities for safe and synergetic wound antibacterial applications. *ACS Nano* **2016**, *10*, 11000−11011.

(35) Luo, J.; Fu, K.; Sun, M.; et al. Phase-mediated heavy metal adsorption from aqueous solutions using two-dimensional layered MoS2. *ACS Appl. Mater. Interfaces* **2019**, *11*, 38789−38797.

(36) Liao, H.-J.; Chen, Y.-M.; Kao, Y.-T.; et al. Freestanding cathode electrode design for high-performance sodium dual-ion battery. *J. Phys. Chem. C* **2017**, *121*, 24463−24469.

(37) Xu, J.; Zhang, J.; Zhang, W.; et al. Interlayer nanoarchitectonics of two-dimensional transition-metal dichalcogenides nanosheets for energy storage and conversion applications. *Adv. Energy Mater.* **2017**, *7*, 1700571.

(38) Liu, Q.; Li, X.; He, Q.; et al. Gram-scale aqueous synthesis of stable few-layered 1T-MoS_2: Applications for visible-light-driven photocatalytic hydrogen evolution. *Small* **2015**, *11*, 5556−5564.

(39) Xie, J.; Zhang, J.; Li, S.; et al. Controllable disorder engineering in oxygen-incorporated MoS_2 ultrathin nanosheets for efficient hydrogen evolution. *J. Am. Chem. Soc.* **2013**, *135*, 17881−17888.

(40) Li, Y.; Chang, K.; Sun, Z.; et al. Selective preparation of 1T-and 2H-phase MoS_2 nanosheets with abundant monolayer structure and their applications in energy storage devices. *ACS Appl. Energy Mater.* **2020**, *3*, 998−1009.

(41) Zhang, X.-H.; Li, N.; Wu, J.; et al. Defect-rich o-incorporated 1T-MoS_2 nanosheets for remarkably enhanced visible-light photocatalytic h_2 evolution over CdS: The impact of enriched defects. *Appl. Catal., B* **2018**, *229*, 227−236.

(42) Sun, B.; Liang, Z.; Qian, Y.; et al. Sulfur vacancy-rich o-doped 1T-MoS_2 nanosheets for exceptional photocatalytic nitrogen fixation over CdS. *ACS Appl. Mater. Interfaces* **2020**, *12*, 7257−7269.

(43) Han, J. H.; Lee, S.; Cheon, J. Synthesis and structural transformations of colloidal 2D layered metal chalcogenide nanocrystals. *Chem. Soc. Rev.* **2013**, *42*, 2581−2591.

(44) He, J.; Hartmann, G.; Lee, M.; et al. Freestanding 1T MoS_2/graphene heterostructures as a highly efficient electrocatalyst for lithium polysulfides in li−s batteries. *Energy Environ. Sci.* **2019**, *12*, 344−350.

(45) Li, Y.; Wang, H.; Xie, L.; et al. MoS_2 nanoparticles grown on graphene: An advanced catalyst for the hydrogen evolution reaction. *J. Am. Chem. Soc.* **2011**, *133*, 7296−7299.

(46) Geng, X. M.; Sun, W. W.; Wu, W.; et al. Pure and stable metallic phase molybdenum disulfide nanosheets for hydrogen evolution reaction. *Nat. Commun.* **2016**, *7*, 10672.

(47) Wu, L.; Dzade, N. Y.; Yu, M.; et al. Unraveling the role of lithium in enhancing the hydrogen evolution activity of MoS_2: Intercalation versus adsorption. *ACS Energy Lett.* **2019**, *4*, 1733−1740.

(48) Xiang, T.; Fang, Q.; Xie, H.; et al. Vertical 1T-MoS_2 nanosheets with expanded interlayer spacing edged on a graphene frame for high rate lithium-ion batteries. *Nanoscale* **2017**, *9*, 6975−6983.

(49) Liu, Y.; Xie, Y.; Liu, L.; et al. Sulfur vacancy induced high performance for photocatalytic h_2 production over 1T@2H phase MoS_2 nanolayers. *Catal. Sci. Technol.* **2017**, *7*, 5635−5643.

(50) Wang, D.; Zhang, X.; Bao, S.; et al. Phase engineering of a multiphasic 1T/2H MoS_2 catalyst for highly efficient hydrogen evolution. *J. Mater. Chem. A* **2017**, *5*, 2681−2688.

(51) Patil, S. B.; Chou, H.-L.; Chen, Y.-M.; et al. Enhanced N_2 affinity of 1T-MoS_2 with a unique pseudo-six-membered ring consisting of n−li−s−mo−s−mo for high ambient ammonia electrosynthesis performance. *J. Mater. Chem. A* **2021**, *9*, 1230−1239.

(52) Zhang, X.; Qiao, X.-F.; Shi, W.; et al. Phonon and raman scattering of two-dimensional transition metal dichalcogenides from monolayer, multilayer to bulk material. *Chem. Soc. Rev.* **2015**, *44*, 2757−2785.

(53) Attanayake, N. H.; Thenuwara, A. C.; Patra, A.; et al. Effect of intercalated metals on the electrocatalytic activity of 1T-MoS_2 for the hydrogen evolution reaction. *ACS Energy Lett.* **2018**, *3*, 7−13.

(54) Calandra, M. Chemically exfoliated single-layer MoS_2: Stability, lattice dynamics, and catalytic adsorption from first principles. *Phys. Rev. B: Condens. Matter Mater. Phys.* **2013**, *88*, 245428.

(55) Li, H.; Zhang, Q.; Yap, C. C. R.; et al. From bulk to monolayer MoS2: Evolution of raman scattering. *Adv. Funct. Mater.* **2012**, *22*, 1385−1390.

(56) Yu, Y.; Nam, G.-H.; He, Q.; et al. High phase-purity 1T'-MoS_2-and 1T'-$MoSe_2$-layered crystals. *Nat. Chem.* **2018**, *10*, 638−643.

(57) Huang, Y.; Sun, Y.; Zheng, X.; et al. Atomically engineering activation sites onto metallic 1T-MoS_2 catalysts for enhanced electrochemical hydrogen evolution. *Nat. Commun.* **2019**, *10*, 1−11.

(58) Castellanos-Gomez, A.; Quereda, J.; van der Meulen, H. P.; et al. Spatially resolved optical absorption spectroscopy of single-and few-layer MoS_2 by hyperspectral imaging. *Nanotechnology* **2016**, *27*, 115705.

(59) Pagona, G.; Bittencourt, C.; Arenal, R.; et al. Exfoliated semiconducting pure 2H-MoS_2 and 2H-WS_2 assisted by chlorosulfonic acid. *Chem. Commun.* **2015**, *51*, 12950−12953.

(60) Tian, L.; Wu, R.; Liu, H. Synthesis of Au-nanoparticle-loaded 1T@2H-MoS_2 nanosheets with high photocatalytic performance. *J. Mater. Sci.* **2019**, *54*, 9656−9665.

(61) Voiry, D.; Goswami, A.; Kappera, R.; et al. Covalent functionalization of monolayered transition metal dichalcogenides by phase engineering. *Nat. Chem.* **2015**, *7*, 45−49.

(62) Mishra, A. K.; Lakshmi, K. V.; Huang, L. Eco-friendly synthesis of metal dichalcogenides nanosheets and their environmental remediation potential driven by visible light. *Sci. Rep.* **2015**, *5*, 15718.

(63) Basu, P.; Chakraborty, J.; Ganguli, N.; et al. Defect-engineered MoS_2 nanostructures for reactive oxygen species generation in the

dark: Antipollutant and antifungal performances. *ACS Appl. Mater. Interfaces* **2019**, *11*, 48179−48191.

(64) Choi, H.; Yang, Z.; Weisshaar, J. C. Single-cell, real-time detection of oxidative stress induced in Escherichia coli by the antimicrobial peptide CM15. *Proc. Natl. Acad. Sci. U. S. A.* **2015**, *112*, E303−E310.

(65) Chang, J. F.; Yeh, J. C.; Ho, C. T.; et al. Targeting ROS and cPLA2/COX2 expressions ameliorated renal damage in obese mice with endotoxemia. *Int. J. Mol. Sci.* **2019**, *20*, 4393.

(66) Dutta, R.; Nenavathu, B. P.; Gangishetty, M. K.; et al. Studies on antibacterial activity of ZnO nanoparticles by ROS induced lipid peroxidation. *Colloids Surf., B* **2012**, *94*, 143−150.

(67) Jackson, S. K.; Thomas, M. P.; Smith, S.; et al. In vivo epr spectroscopy: Biomedical and potential diagnostic applications. *Faraday Discuss.* **2004**, *126*, 103−117.

(68) Su, H.-L.; Chou, C.-C.; Hung, D.-J.; et al. The disruption of bacterial membrane integrity through ROS generation induced by nanohybrids of silver and clay. *Biomaterials* **2009**, *30*, 5979−5987.

(69) Maitra, U.; Gupta, U.; De, M.; et al. Highly effective visible-light-induced h_2 generation by single-layer 1T-MoS$_2$ and a nano-composite of few-layer 2H-MoS$_2$ with heavily nitrogenated graphene. *Angew. Chem., Int. Ed.* **2013**, *52*, 13057−13061.

(70) Chen, Y.; Zhang, G.; Ji, Q.; et al. Triggering of low-valence molybdenum in multiphasic MoS$_2$ for effective reactive oxygen species output in catalytic fenton-like reactions. *ACS Appl. Mater. Interfaces* **2019**, *11*, 26781−26788.

(71) Xu, L.; Tetreault, A. R.; Pope, M. A. Chemical insights into the rapid, light-induced auto-oxidation of molybdenum disulfide aqueous dispersions. *Chem. Mater.* **2020**, *32*, 148−156.

(72) Abinaya, R.; Archana, J.; Harish, S.; et al. Ultrathin layered MoS$_2$ nanosheets with rich active sites for enhanced visible light photocatalytic activity. *RSC Adv.* **2018**, *8*, 26664−26675.